Variability of the snowline altitude in the eastern Tibetan Plateau from 1995 to 2016 using Google Earth Engine

Chang Liu,[a,b] Zhen Li,[a,*] Ping Zhang,[a] Bangsen Tian,[a] Jianmin Zhou,[a] and Quan Chen[a]

[a]Chinese Academy of Sciences, Aerospace Information Research Institute, Key Laboratory of Digital Earth Science, Beijing, China
[b]University of Chinese Academy of Sciences, Beijing, China

Abstract. The glacier snowline can be used as an indicator of a glacier's equilibrium line, which is a pivotal parameter for studying the effect of climate change on glaciers. However, the relationship between snowline altitudes (SLAs) and climatic regime, as well as the comparison between different glacier types, has received less attention. Using Google Earth Engine, we first developed an automated algorithm that employs the Otsu thresholding method to distinguish snow-covered areas from clean ice on a near-infrared band of Landsat imagery available from 1995 to 2016 and further to delineate glacier SLAs in the three regions of the eastern Tibetan Plateau (TP). The three study regions, Sepu Kangri (maritime), Bu'Gyai Kangri (continental), and western Qiajajima (continental), in the eastern TP have different climate regimes and are on a latitudinal transect from south to north. We then investigated the impacts of climatic factors on the SLA and its variability over the period studied. The results over the eastern TP indicate that (1) the SLA increased by 94, 55, and 49 m from south to north during the 22-year period, with the SLA variations of maritime glaciers being the most pronounced; (2) the southern maritime glaciers were mainly affected by precipitation, whereas the northern continental glaciers were influenced by temperature. Owing to the difference in primary climatic factors affecting snowlines, continental glaciers were found to have higher SLAs on the south slope, whereas maritime glaciers had higher SLAs on the north slope. [DOI: 10.1117/1.JRS.15.048505]

Keywords: snowline altitude; spatiotemporal variability; local climate regime; Otsu thresholding method; Google Earth Engine.

Paper 210445 received Jul. 14, 2021; accepted for publication Nov. 29, 2021; published online Dec. 11, 2021.

1 Introduction

Glaciers are natural water reservoirs[1,2] and are of vital importance to hydropower generation and hydrological models.[3,4] They are important indicators of climate variation[5–7] because fluctuations in climate can cause changes in their areal extent, volume, mass balance,[8–10] and equilibrium line altitude (ELA).[11] Mass balance and ELA, as direct reflections of climate change, integrate the competing effects of snow accumulation and ablation processes.[12]

Field-based mass balance measurements are time-consuming, and it is difficult to obtain adequate representation at the scale of a mountain chain.[13] In contrast, satellite imagery allows for spatially consistent temporal reconstruction of glacier changes over recent decades.[14,15] The World Glacier Monitoring Service provides information for glaciers globally through direct field measurements and satellite images combined with geographic information science techniques.[16] The Global Land Ice Measurements from Space project was established to acquire satellite-spectral images of the world's glaciers and analyze them for changes in extent and other characteristics.[17] Some glacier studies[18–20] have suggested that the snowline altitude (SLA) is

*Address all correspondence to Zhen Li, lizhen@radi.ac.cn

equivalent to the minimum elevation of perennial snow cover on a glacier near the end of the ablation period, making it a good proxy for the ELAs of mid-latitude glaciers. Regional SLA estimation using satellite imagery, when measured at the end of the ablation period, can be approximated by the lower boundary of the continuous snow-covered area (SCA).[21–23] Remotely sensed snow products have been applied for snowline observations; for example, Tang et al.[24,25] monitored the spatiotemporal patterns of the SLAs over High Mountain Asia using cloud-removed Moderate Resolution Imaging Spectroradiometer (MODIS) fractional snow cover data with 500 m resolution. Various methods[26–28] have also been developed for determining SLAs by applying various spectral band ratios to higher-resolution imagery. For instance, Hu et al.[29] and Girona-Mata et al.[12] delineated the snowlines for each Landsat scene by identifying the border between snow-covered and snow-free areas, which was determined by applying thresholds on the normalized difference snow index (NDSI)[30] in European mountains and the Himalayan catchment, respectively. However, the same threshold might not perform well in all regions because of highly variable cloud conditions, and it is essential to find an automated algorithm with the threshold adjusted to the local circumstances for each glacier individually.

Moreover, SLA and its spatial and interannual variability are known to be linked with the climate setting with sensitivity varying by region, such as in the western Himalayas[31] and in tropical and subtropical regions.[32] Further knowledge of the SLA controlling mechanisms plays a key role in assessing the potential application of the SLA to climate reconstruction and hydrological processes, especially in mountainous areas. The Tibetan Plateau (TP), referred to as the Third Pole, is one of the most sensitive areas responding to regional and global climate changes. Variations in glacier SLA in the TP have, therefore, received increasing attention. It encompasses 36,102 glaciers with a total area of $49,688\ km^2$,[33] and the glacier types in the plateau are mainly divided into continental and maritime glaciers.[34] The location of maritime glaciers is limited to the southeastern TP, whereas continental glaciers are widely distributed in other regions of the TP.[35,36] However, little is known about the connection between SLAs and climatic regimes, especially in the eastern TP, and there is a lack of comparisons between different glacier types.

In this context, this study focuses on the following two objectives. The first is to develop an automated approach that implements the Otsu threshold method[37] on a near-infrared (NIR) band to derive the snowline at a 30-m resolution from the 22-year time series of historic Landsat scenes in the eastern TP. The second is to investigate the connection between SLAs and climate regimes in different regions and describe the climatic mechanisms governing SLA dynamics for different glacier types in the eastern TP. The remainder of this article is organized as follows. Section 2 introduces the study area and datasets. The automated algorithm for extracting SLA is demonstrated in Sec. 3. In Sec. 4, the SLA and its variability during the 22-year period are presented. Section 5 discusses the linkage between the SLA interannual variability on the north and south slopes of different glaciers and the local climate conditions. Finally, Sec. 6 summarizes this study.

2 Study Area and Data

2.1 *Study Area*

To explore the relationship between local climate change and glacier SLA variation, three study areas distributed across the eastern TP were selected. These study sites include the regions of Sepu Kangri (SK; central location: 30.90°N, 93.78°E), Bu'Gyai Kangri (BK; central location: 31.82°N, 94.70°E), and western Qiajajima (WQ; central location: 33.58°N, 95.02°E), along a latitudinal transect from south to north (Fig. 1). Glaciers in the SK region are considered to be the maritime type,[38] whereas those in the other two regions are the continental type.[39]

2.2 *Google Earth Engine and Landsat Imagery*

The Google Earth Engine (GEE) cloud computing platform[40] not only provides a large number of Landsat images in raw digital number (DN) form and top-of-atmosphere and surface reflectance orthorectified formats but also offers interactive exploration to quickly determine the

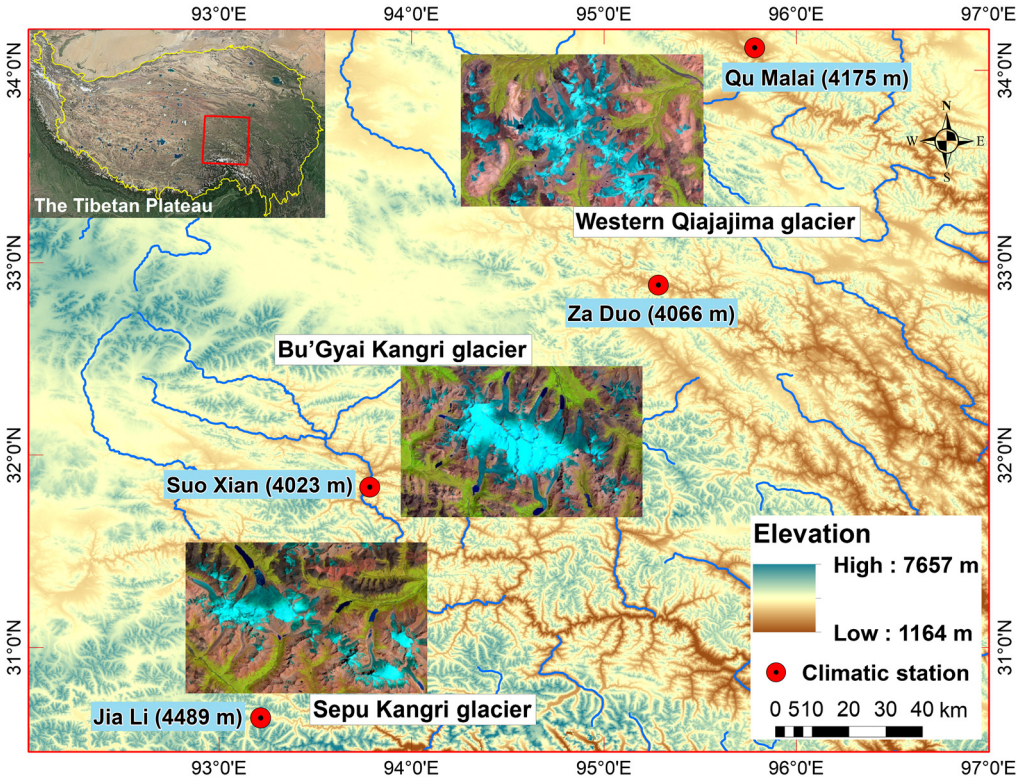

Fig. 1 Locations of glaciers discussed in the paper. The three regions include the SK, BK, and WQ regions from south to north in the eastern TP (the upper left inset is the TP, and the red rectangle includes the study area). Red points represent climatic stations, which include Jia Li, Suo Xian, Za Duo, and Qu Malai from south to north. Mosaic 30-m Advanced Spaceborne Thermal Emission and Reflection Radiometer Global Digital Elevation Model (ASTER GDEM) as background.

spatial coverage of the study area and the temporal extent of satellite image collections.[40] As a cloud-based platform for mapping applications and data analysis, GEE enables monitoring long-term SLA variability in mountainous areas at 30-m spatial resolution. Because Landsat images taken at the end of the ablation season in the eastern TP were greatly affected by clouds, a total of 21 Landsat scenes acquired from 1995 to 2016 were finally selected for this study (Table 1). In addition to the Landsat product, high-resolution Sentinel-2 imagery under cloudless conditions was adopted to evaluate the SLA results.

2.3 *Meteorological Data*

Four meteorological stations within this study area record data such as daily air temperature and precipitation. Through these station records obtained from the National Meteorological Information Centre (NMIC),[41] the effects of these climatic variables on SLA can be investigated. To ensure that the dates of satellite images and meteorological measurements were in good agreement during the study period, only the mean temperature and precipitation at the four meteorological stations at the end of the ablation period (July to August) from 1995 to 2016 were analyzed. Station locations are shown in Fig. 1, and their location details are given in Table 2. These data suggested that the mean temperature at the four stations increased during the 22-year period and that the precipitation increased at each station except for Jia Li.

2.4 *DEM and Glacier Outlines*

The DEM scenes were used to extract SLA ranges. The ASTER GDEM, created from ASTER imagery, was released in 2009.[42] It has good spatial consistency with Landsat, with a horizontal resolution of 30 m and a vertical accuracy of ~20 m.[13,43] The Randolph Glacier Inventory

Table 1 Information on satellite images used for SLA measurements in GEE (thematic mapper, TM; enhanced thematic mapper, ETM+; operational land imager, OLI).

Region	Date	Sensor	Resolution (m)	Path/row	Cloud cover (%)
SK	July 25, 1995	TM	30	136/39	29
	July 22, 2000	TM	30	136/39	42
	August 5, 2002	ETM+	30	136/39	48
	August 8, 2006	TM	30	136/39	68
	August 11, 2013	OLI	30	136/39	20
	August 19, 2016	OLI	30	136/39	8
BK	July 25, 1995	TM	30	136/38	8
	July 17, 1998	TM	30	136/38	23
	July 22, 2000	TM	30	136/38	24
	August 5, 2002	ETM+	30	136/38	31
	August 8, 2006	TM	30	136/38	10
	August 6, 2011	TM	30	136/38	37
	August 19, 2016	OLI	30	136/38	1
WQ	July 25, 1995	TM	30	136/37	6
	July 17, 1998	TM	30	136/37	0
	July 22, 2000	TM	30	136/37	17
	August 5, 2002	ETM+	30	136/37	22
	August 8, 2006	TM	30	136/37	10
	August 6, 2011	TM	30	136/37	13
	August 11, 2013	OLI	30	136/37	3
	August 19, 2016	OLI	30	136/37	5

Table 2 Information and climatic conditions at meteorological stations. Mean air temperature (°C) and precipitation (mm) are shown, as well as their 22-year trend (22 yr^{-1}).

Station	Coordinates		Mean air temperature (°C 22 yr^{-1})	Mean precipitation (mm 22 yr^{-1})
	Latitude (deg)	Longitude (deg)		
Jia Li	30.633	93.216	8.8 (+1.1)	136.9 (−9.0)
Suo Xian	31.833	93.783	11.9 (+1.1)	113.4 (+13.3)
Za Duo	32.883	95.283	11.4 (+1.2)	102.2 (+11.5)
Qu Malai	34.116	95.783	9.5 (+1.6)	87.9 (+15.7)

(RGI)[17,44] is a global inventory of glacier outlines freely available from the website.[45] Here, 26 glaciers larger than 1 km^2 in the three regions were selected as the research objects. Not all glaciers in the regions have a proper name; exceptions include Zuxuehui, Zhonggeimanong, Poge, and Beijia. Therefore, for the purpose of minimizing confusion, these 26 glaciers were identified using the names Glacier-A to Glacier-Z (A-Z glaciers), with their attributes shown in Table 3.

Table 3 Mean SLA and spatiotemporal changes on each glacier in the three regions from 1995 to 2016 (latitude, longitude, glacier area, max Z, and aspect come from RGI6.0).

Glacier ID	Latitude (deg)	Longitude (deg)	Area (km^2)	Max Z (m)	Aspect	Mean SLA (m)	SD (m)	ΔSLA (m 22 yr^{-1})
G093821E30892N (A)	30.892	93.820	2.59	6407	SE	5670	25	1
G093849E30898N (B)	30.898	93.849	2.45	6100	S	5501	10	123
G093813E30919N (C)	30.919	93.813	20.41	6893	N	5557	46	219
G093862E30917N (D)	30.917	93.862	5.60	6110	NE	5537	36	46
G093872E30896N (E)	30.895	93.871	3.04	6060	E	5396	09	188
G093943E30855N (F)	30.855	93.943	8.00	6204	N	5573	22	98
G093982E30849N (G)	30.848	93.982	5.16	6106	SE	5522	50	37
G093752E30923N (H)	30.922	93.751	5.94	6505	NW	5747	18	94
Bu'Gyai Kangri 4674 (I)	31.837	94.626	4.33	6129	W	5733	34	−36
Zuxuehui (J)	31.807	94.667	35.49	6257	SW	5649	27	58
Poge (K)	31.782	94.728	22.27	6261	SW	5670	19	129
Zhonggeimanong (L)	31.847	94.684	15.37	6226	N	5531	21	71
West Beijia (M)	31.839	94.720	9.42	6251	N	5534	25	31
Beijia (N)	31.824	94.745	13.60	6244	NE	5523	44	46
East Beijia (O)	31.816	94.775	10.08	6107	NE	5389	23	150
CN5K427A0047 (P)	33.584	94.931	7.50	5825	N	5456	33	14
CN5K427A0045 (Q)	33.588	94.961	8.62	5759	N	5412	40	49
CN5K427A0023 (R)	33.558	95.010	1.60	5756	NE	5471	17	3
CN5K427A0020 (S)	33.543	95.031	3.10	5699	N	5394	08	32
CN5L412G0031 (T)	33.559	94.803	1.99	5631	NW	5393	15	−115
CN5L412G0071 (U)	33.558	94.815	3.41	5593	SE	5464	23	45
CN5L412G0084 (V)	33.566	94.922	3.08	5832	SW	5480	34	8
CN5L412G0086 (W)	33.555	94.945	3.67	5736	SW	5484	39	−119
CN5L412I0010 (X)	33.563	94.985	2.31	5704	SW	5389	16	−44
CN5L412I0014 (Y)	33.537	95.012	2.62	5722	SW	5416	17	37
CN5L412I0025 (Z)	33.523	95.038	4.53	5726	NE	5433	26	40

3 Methods

Significant differences in spectral reflectance characteristics are the basis of image classification. Both snow and ice have high spectral reflectance in the visible bands, whereas in the NIR band, the reflectance of clean ice gradually decreases and is less than the reflectance of snow.[43,46] The Otsu thresholding method is reliable in that the two classes are automatically distinguished by the threshold that maximizes the thresholding function,[47] thus realizing the distinction between snow cover and clean ice surfaces in the NIR band.[48] Subsequently, the discontinuously distributed snow that may have been more influenced by shadowing and local effects[23] was removed, and the continuous SCA of each glacier was extracted as the primary snow region. The lowest

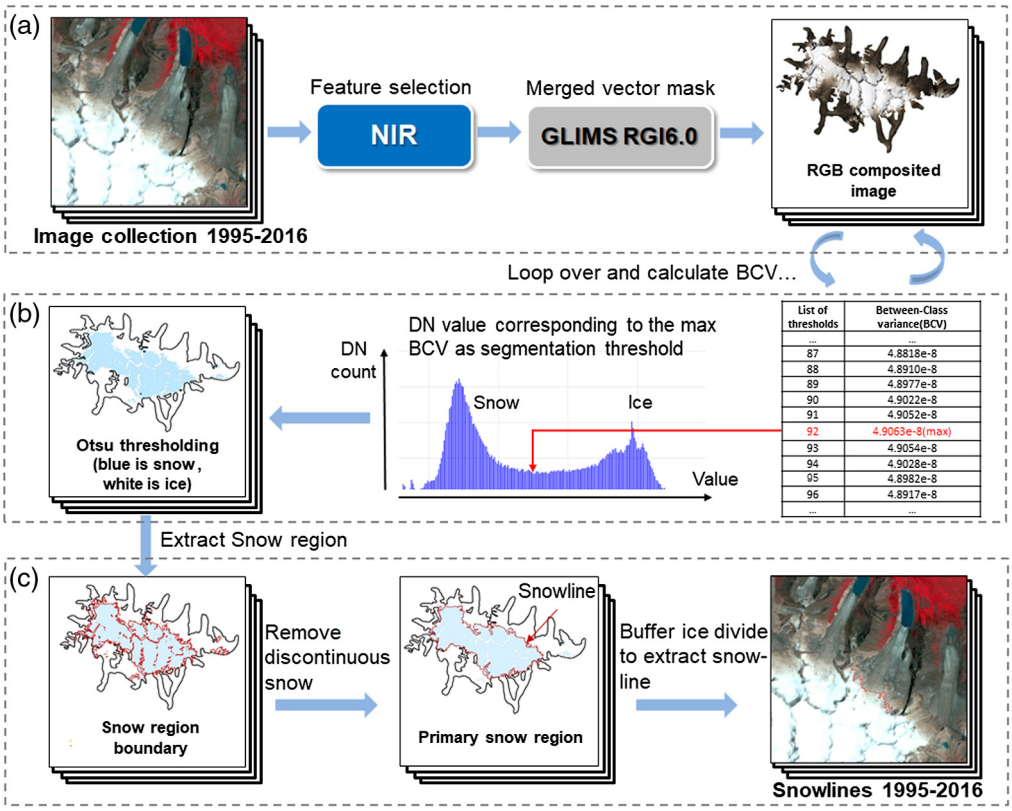

Fig. 2 Framework diagram of SLA extraction from Landsat images and DEM data using GEE. (a) Select Landsat images, clip them using glacier outlines, and determine NIR band as the optimal feature; (b) discriminate snow from clean ice using Otsu thresholding method; and (c) delineate primary snow region and extract snowlines after negative buffering.

boundary of the primary snow region was considered to be the position of the glacier snowline, and the SLA of each glacier was obtained using ASTER GDEM (Fig. 2).

3.1 *GEE-Based Landsat Imagery Selection*

All Landsat images from 1995 to 2016, derived from the Landsat TM, ETM+ and OLI satellite instruments, were filtered on GEE through the following three criteria:[13,23]

(a) Spatiotemporal criterion: in the study area, Landsat scenes of July and August from 1995 to 2016 were selected as the seasonal SCA achieved its minimum value during this period.

(b) Regional cloud cover: one of the Landsat image metadata attributes, "CLOUD COVER," represents the cloud cover of the total image rather than the study area. Thus, the cloud percentage within the study area (i.e., regional cloud amount) was calculated by the "simple cloud score" function and stored in the image metadata as a new attribute, "regional cloud cover." If CLOUD_COVER > 70% or regional cloud cover >40%, the image was discarded.

(c) Minimum seasonal snow extent: based on the above criteria, the NDSI with a threshold of 0.4[30] was also utilized to calculate the seasonal snow coverage for each scene, and the percentage was stored in the image metadata as a new attribute, "seasonal snow extent." The image with the minimum seasonal snow extent was finally selected as the optimal imagery to delineate the snowline.

Filtering Landsat products through these three criteria yielded only 21 images for the study area from 1995 to 2016 (detailed information in Table 1). One possible reason is the fact that satellite imagery under clear sky conditions is not available in every year, especially Landsat images affected by the failure of the Landsat-7 scan-line corrector after May 31, 2003.

3.2 *Feature Selection before Implementing the Otsu Method*

From previous studies, the calculation of band ratios such as NIR/shortwave infrared (SWIR), red/SWIR, or NDSI has proven successful in mapping glacier extent.[49,50] However, these features map all ice and snow-covered surfaces without separating snow from clean ice, and the threshold must be chosen manually depending on the scene characteristics in different regions.[50] De Angelis[48] took a histogram of Glacier Tyndall to separate ice and snow by applying the thresholding function to NIR because the spectral reflectance characteristics differ greatly between snow and clean ice within glacierized areas in the NIR. Rabatel et al.[13] compared different band combinations and band ratios to facilitate the identification of snowlines on satellite images and showed that TM4 (NIR) with a threshold of 120 was the most appropriate for SLA retrieved from satellite images. Considering that the Otsu thresholding method performs best on the optimal feature, we compared the histogram distributions of different band combinations to find this feature. As shown in Fig. 3, the double peaks of snow and clean ice in the NIR were indeed more obvious than those of other features. Therefore, the Otsu thresholding method was applied to the NIR band to automatically distinguish SCAs from clean ice [Fig. 2(a)].

3.3 *Otsu Thresholding Method*

The Otsu thresholding method uses a gray histogram in a spectral band to divide the images into target and background with a binary image as output. The segmentation threshold is adaptively obtained by calculating the between-class variance (BCV). However, this method is sensitive to the size of the target classification and noise. If many nonglacierized surroundings are considered to be the background (e.g., vegetation, land, and water) in one image, the DN value distribution is discrete, which causes the within-class variance (WCV) of the background to be relatively large. In this case, the segmentation threshold will be closer to the DN value of the background; thus, the background is likely misclassified into the target. Hence, neighboring glaciers with overlapping boundaries in RGI were merged into one validity vector mask and uploaded to GEE for clipping Landsat images [Fig. 2(a)] to reduce the complexity of the image and prevent misclassification caused by nonglacierized surroundings.

As displayed in Fig. 2(b), the Otsu thresholding method will automatically search using DN values corresponding to the maximum BCV as the segmentation threshold to produce snow/ice classification. The key steps to implementing this method in GEE are as follows: (a) creating a list to store all thresholds; (b) computing weight and average DN values of target and background in the NIR band, respectively; (c) according to Eq. (4), looping over thresholds to calculate BCV for each; and (d) obtaining the maximum value of BCV. The value in the threshold list corresponding to the maximum BCV is used as the segmentation threshold for the image to produce clean ice and snow classification. The entire process of the Otsu thresholding method was employed for each Landsat image individually:

$$w_b = n_b/N, \quad w_t = n_t/N, \tag{1}$$

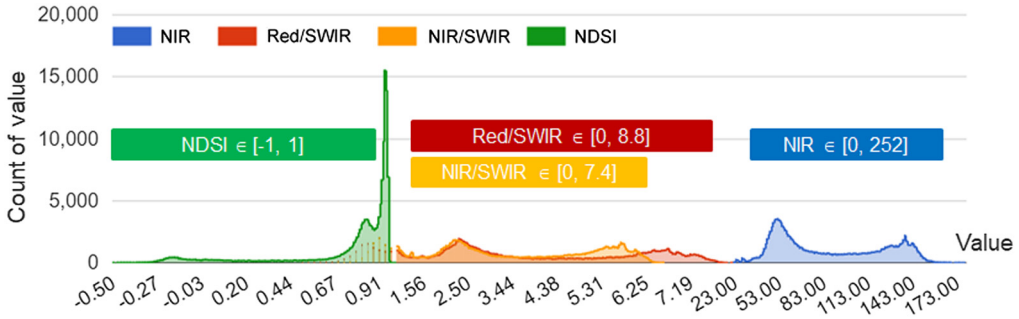

Fig. 3 Taking the Beijia glacier of the BK region as an example, the histogram distributions of different features (i.e., NIR, red/SWIR, NIR/SWIR, and NDSI) are displayed. The Landsat imagery used here was acquired on August 19, 2016.

$$w_b + w_t = 1, \tag{2}$$

$$w_b\mu_b + w_t\mu_t = \mu, \tag{3}$$

$$\sigma_B^2 = \sigma^2 - \sigma_W^2 = w_b(\mu_b - \mu)^2 + w_t(\mu_t - \mu)^2 = w_b w_t(\mu_b - \mu_t)^2, \tag{4}$$

where n_b is the pixel count of the background, n_t is the pixel count of the target, N is the overall pixel count in one image, w_b is the background weight, w_t is the target weight, μ_b is the average background DN value, μ_t is the average target DN value, μ is the overall average DN value, σ_B^2 is BCV, σ_W^2 is WCV, and σ^2 is the total variance.

3.4 *Snowline Delineation*

To delineate the snowline position after the Otsu thresholding method, the largest continuous SCA of each glacier region was calculated as the primary snow region [e.g., the area surrounded by the red line in Fig. 2(c)] with the boundary of this region representing the snowline position. Moreover, the topography is known to be extremely steep in these regions, and glaciers are often disconnected from steep upper faces, which affects the distribution of snow cover and the location of the snowline. Therefore, a negative edge buffer,[51,52] with a buffer size of −200 m, removed the steep part of the glacier and ensured the stability and reliability of the snowline. Finally, snowlines were mapped for each of the 26 glaciers with selected Landsat imagery during the study period overlain on the ASTER GDEM to determine the altitude ranges of the snowlines in the three regions. To investigate whether SLA extraction performs better with the negative buffer, the SLA distribution before and after buffering was compared (Fig. 4). Figure 2(c) shows the postprocessing in GEE after the Otsu thresholding method to detect the snowline positions by the primary snow region and negative buffer.

4 Results

Due to the lack of any field-based measurements, we extracted SLA through manual interpretation and the Otsu thresholding method from the 10-m Sentinel-2 image (August 12, 2016) as the appropriate reference data to assess the accuracy of the SLA derived from Landsat (August 19, 2016). Although the images are not from the same date, the Sentinel-2 image, compared with Landsat, has a higher resolution available for snowline accuracy assessment. In Sentinel-2

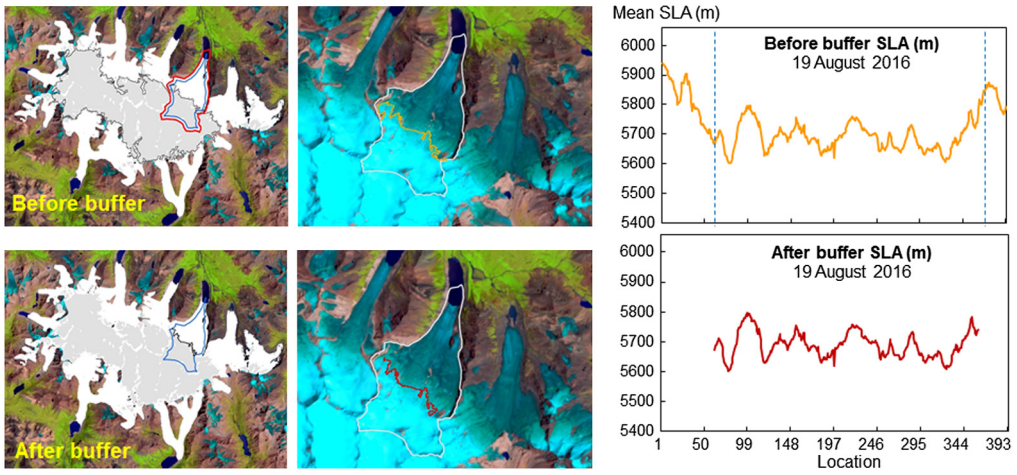

Fig. 4 Comparison between snowline delineation before (upper) and after (lower) buffering, where a negative buffer removes special values at the steep parts of the glacier. In the left column, the red glacier outline is the original, and the blue glacier outline is after the negative buffer (−200 m). The standard variance of SLA extraction decreases from 125 to 41 m. The background imagery was acquired from Landsat 8 on August 19, 2016, and is composed of SWIR, NIR, and red bands.

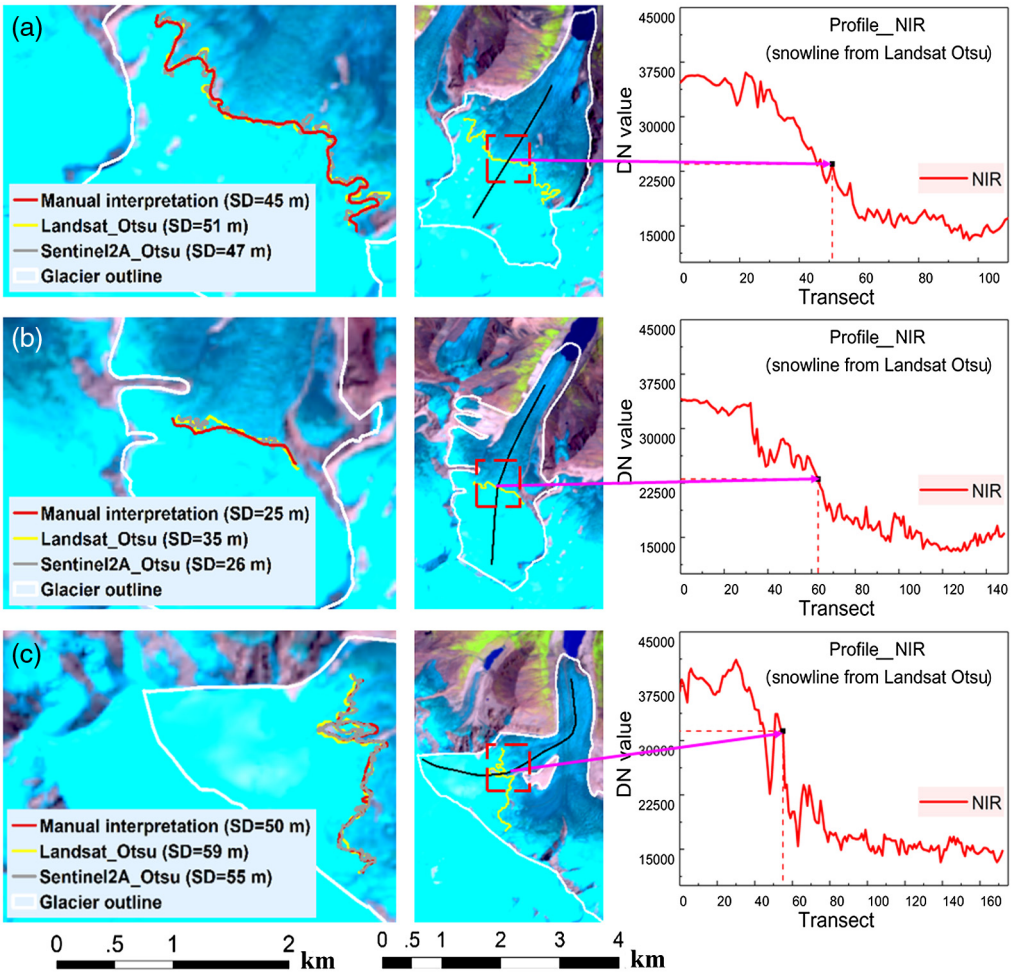

Fig. 5 Mean SLA and its standard deviation were calculated for each glacier: (a) Beijia Glacier, (b) West Beijia Glacier, and (c) Zhonggeimanong Glacier. The position of the snowline indicated by the arrow corresponds to the position where the DN value suddenly changes in the spectral profile. The background is Landsat imagery (August 19, 2016, and RGB is SWIR, NIR, and red).

imagery, clouds obscured partial glaciers in the BK region, and only three cloudless glaciers were available for reference in 2016 (Beijia, West Beijia, and Zhonggeimanong as a, b, c in Fig. 5). The standard deviation (SD) for the mean SLA presented here is the elevation range of individual glacier snowlines and is used to estimate the uncertainty error for each SLA.[13] For the three glaciers in the BK region, the uncertainty range of SLAs was between 35 and 59 m. As shown in Fig. 5, the position of the snowline obtained by applying the Otsu thresholding method to the Landsat scenes was close to that drawn by manual interpretation on the higher-resolution Sentinel-2 imagery, indicating that the Otsu thresholding method performs well in delineating the snowline of each glacier.

Consequently, SLAs were calculated for 26 glaciers larger than 1 km^2 in the three regions: 8 glaciers in the SK region, 7 glaciers in the BK region, and 11 glaciers in the WQ region. The results (Table 3) include the mean SLAs and SDs monitored with Landsat images in the three regions and the rate of SLA change over time, which may be indicators of climate and annual climate variation.

In the period of 1995 to 2016, the mean SLAs of all glaciers in the SK region were on the rise [Fig. 6(a)], with increases ranging from 1 to 219 m. Among them, Glacier-C had the largest glacier area, the highest elevation, and a temporal change in SLA (ΔSLA) of 219 m, the largest change in the study period. Glacier-A had the smallest ΔSLA (1 m). The highest mean SLA of all glaciers was on Glacier-H (5747 ± 18 m) in the SK region, which had the second highest

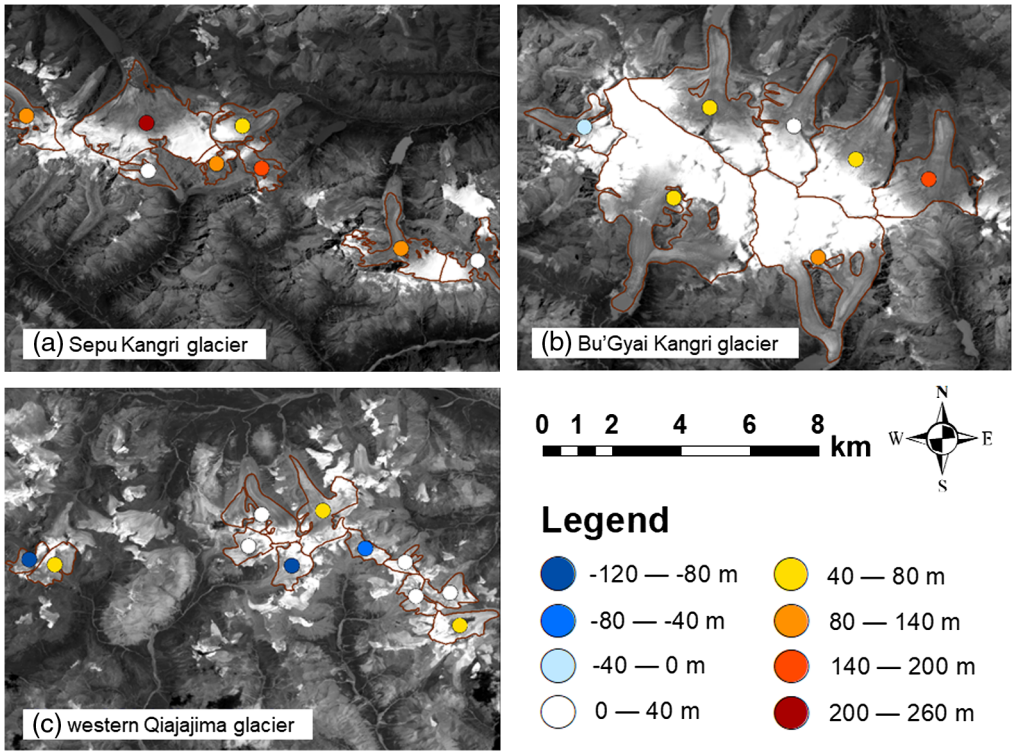

Fig. 6 SLA variability of the three regions from 1995 to 2016: (a) SK, (b) BK, and (c) WQ. The ΔSLA values for individual glaciers are shown as colored circles, with dark red circles indicating the largest SLA rise and dark blue circles indicating the largest SLA descent.

elevation among all glaciers. The lowest mean SLA was on Glacier-E (5396 ± 09 m), which had the lowest elevation.

Except for the descending trend of Glacier-I in the BK region from 1995 to 2016, the mean SLAs of other glaciers were on the rise [Fig. 6(b)]. Glacier-M, which had a slightly smaller glacier area and higher elevation, had the smallest ΔSLA (31 m). Glacier-O, with the lowest elevation, had the largest ΔSLA (150 m). The maximum and minimum values of ΔSLA were found to appear in the north and northeast of the BK region, but ΔSLA variations were different, which may be related to the elevation of different glaciers. The highest mean SLA among all glaciers in the BK region was on Glacier-I (5733 ± 34 m), and the lowest was on Glacier-O (5389 ± 23 m).

Within the WQ region, the mean SLAs of different glaciers varied from 1995 to 2016 [Fig. 6(c)]. Glacier-R, with the smallest area, had the smallest ΔSLA (3 m). In contrast, Glacier-W, with the largest ΔSLA, descended 119 m. The highest mean SLA was on Glacier-W (5484 ± 39 m), and the lowest mean SLA in the WQ region was on Glacier-X (5389 ± 16 m). Although three glaciers (e.g., Glacier T, W, X) had negative trends, glaciers with increasing SLA (>30 m) were also found in the WQ region.

5 Discussion

Considering all glaciers in each region to be one group, the mean SLAs of the three regions in the eastern TP from 1995 to 2016 were 5571 m (SK), 5580 m (BK), and 5435 m (WQ) from south to north, respectively. The interannual variability in SLA exhibited increasing trends, with increases of 94 m 22 yr^{-1}, 55 m 22 yr^{-1}, and 49 m 22 yr^{-1} from south to north. Clearly, maritime glaciers in the SK region were more sensitive to the local monsoon climate, with the most pronounced variation in SLA ($R^2 = 0.56$). Glaciers in the WQ region were continental glaciers and had small variations in SLA. The BK region was located in the transition zone between continental glaciers and maritime glaciers, and the SLA changed 55 m during the period studied.

The relationship between the interannual SLA variability and regional climate changes in the eastern TP is worthy of further exploration (note that significance tests were conducted at the 95% confidence level). The orientations of glaciers in the eastern TP, divided into south and north slopes (the south slope is the sunny slope; the north slope is the shady slope), may influence SLA due to temperature and precipitation differences. These climatic factors were derived from data collected at four meteorological stations. Among them, the mean temperatures of the three regions during the end of the ablation period were 10.4°C, 11.7°C, and 10.5°C, and the mean precipitation totals were 125.2, 107.8, and 95.1 mm from south to north.

5.1 *Effect of Climatic Factors on SLA in the SK Region*

The SK region is located on the east side of Mount Nyenchen Tanglha and is obviously affected by the southwest monsoons from the Indian Ocean in summer.[53] Glaciers in this area are typically maritime in that they receive a large amount of water vapour (e.g., precipitation 125.2 mm). For the entire SK region, the precipitation was statistically significant with respect to the SLA variation [Fig. 7(b); $R^2 = 0.66$, $P < 0.05$], and the temperature very likely also had an effect on the SLA changes because of the relatively large correlation coefficient [Fig. 7(a); $R^2 = 0.64$, $P < 0.10$]. For the north and south slopes, the interannual variation in SLA was related to different climatic factors. Specifically, the SLA variation on the north slope may be statistically significant in terms of temperature [Fig. 7(c); $R^2 = 0.70$, $P < 0.05$]. Both temperature and precipitation on the north slope increased in 2006, but the increase in temperature suppressed the influence of the increase in precipitation on the SLA variation, resulting in a rapid rise in SLA. In contrast, precipitation had a greater impact on the SLA of the south slope [Fig. 7(d); $R^2 = 0.56$, $P < 0.10$]. The SLA rose when the temperature decreased in 2013, which was attributable to the decrease in precipitation.

Maritime glaciers were distributed in areas with abundant precipitation and humid climates, where SLA variability was more significantly affected by precipitation. Although the highest elevation of the region ranged from 6060 to 6893 m, the mean SLA in the SK region was

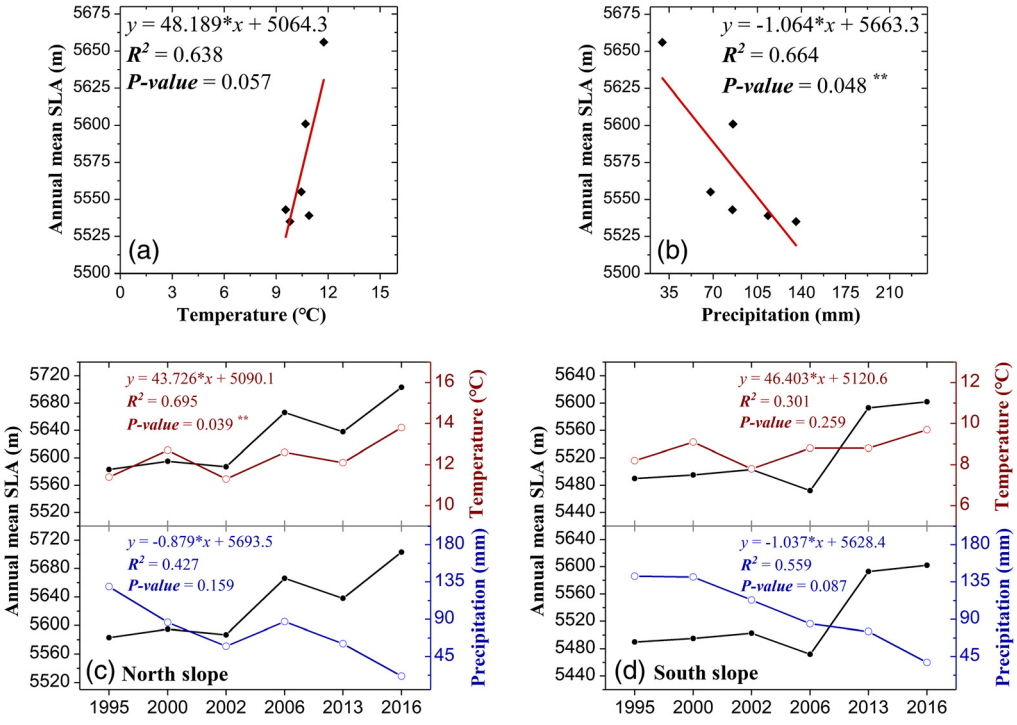

Fig. 7 Scatter plots show the relationships between mean SLAs and climatic factors such as (a) air temperature and (b) precipitation in the SK region from 1995 to 2016. Linear analyses between the annual mean SLAs and climatic factors on different slopes: (c) north slope and (d) south slope. ** indicates that the linear analysis is significant at the 95% confidence level.

5571 m. Furthermore, the primary climatic factors affecting SLA changes on the north and south slopes were different, and the mean SLA on the south slope (5524 m) was significantly lower than that on the north slope (5628 m).

5.2 *Effect of Climatic Factors on SLA in the BK Region*

The BK region lies in the transitional zone from maritime to continental glaciers, which are dominated by southeast and east monsoons during the precipitation season.[39] In the analysis of the transitional region, the SLA variations during the study period were much more affected by temperature [Fig. 8(a); $R^2 = 0.57$, $P < 0.05$] than precipitation. Unlike maritime glaciers in the SK region, the glacier SLAs on the north and south slopes responded to the climatic factors consistently. When the temperature and precipitation both increased in 1998, the SLA of the north slope rose [Fig. 8(c)], revealing that the temperature had a more significant influence on the SLA than precipitation. Likewise, a tighter linkage between SLA variations and temperature was also found on the southern slope [Fig. 8(d); $R^2 = 0.58$, $P < 0.05$]. Specifically, the mean temperature on the south slope (11.9°C) was higher than that on the north slope (11.4°C), and the mean SLA (5685 m) was also higher than that on the north slope (5496 m). As an independent plateau with a maximum elevation of 6261 m, the mean SLA of the entire BK region reached 5580 m, which was the highest altitude of the snowline over the three regions in the eastern TP.

5.3 *Effect of Climatic Factors on SLA in the WQ Region*

The southern and southwest monsoons prevail in the southern TP at 30°N in summer and gradually weaken at 30°N to 35°N, whereas westerlies prevail north of 35°N.[54] The northernmost glaciers in the WQ region, located to the southeast of Qinghai Province, were spatially affected by westerlies, and there was a certain correlation between the SLA variations and temperature in this area [Fig. 9(a); $R^2 = 0.41$, $P < 0.10$]. Similarly, the SLAs on the south slopes were more

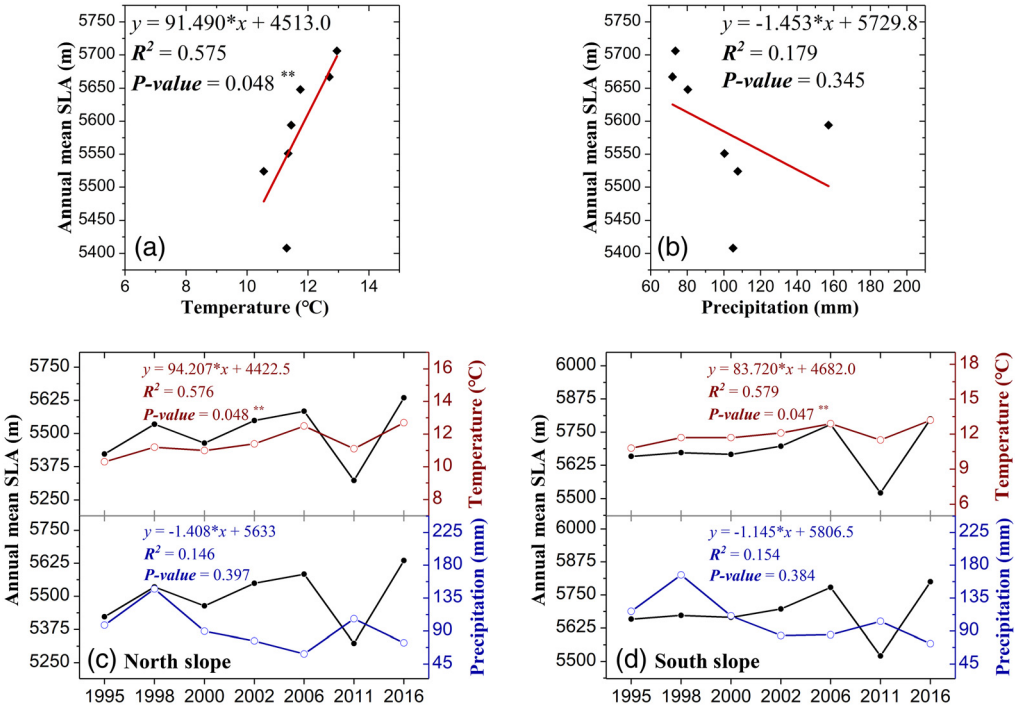

Fig. 8 Scatter plots show the relationships between mean SLAs and climatic factors such as (a) air temperature and (b) precipitation in the BK region from 1995 to 2016. Linear analyses between the annual mean SLAs and climatic factors on different slopes: (c) north slope and (d) south slope. ** indicates that the linear analysis is significant at the 95% confidence level.

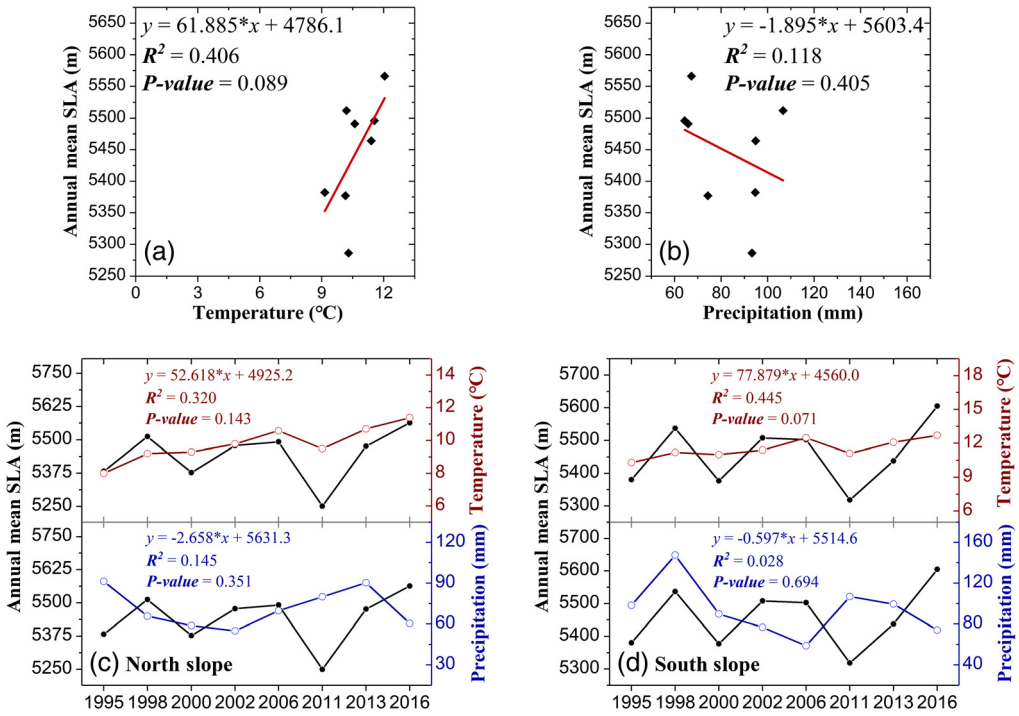

Fig. 9 Scatter plots show the relationships between mean SLAs and climatic factors such as (a) air temperature and (b) precipitation in the WQ region from 1995 to 2016. Linear analyses between the annual mean SLAs and climatic factors on different slopes: (c) north slope and (d) south slope.

sensitive to temperature [Fig. 9(d); $R^2 = 0.45$, $P < 0.10$] than to precipitation. From 2011 to 2016, the temperature increased annually, whereas the precipitation decreased year by year, which made the position of the snowline rise continuously to reach the maximum during this period. Although the SLA on the north slope [Fig. 9(c)] did not pass the significance tests for temperature and precipitation, SLAs exhibited a clear change tendency under the integrated influence of these two climatic factors. For example, the decrease in temperature and increase in precipitation in 2011 caused the SLA to reach a minimum value during the study period, whereas the opposite meteorological variations led to an upward turn of SLA in 2016.

Obstructed by the extreme peaks of the Himalayas and Mount Nyenchen Tanglha, the precipitation in the WQ region was much less than those in the other two areas, and the interannual SLA variability of the continental glaciers was relatively affected by temperature. The difference in mean SLAs was slight, with 5433 m on the north slope and 5438 m on the south slope.

In addition, the spatial and temporal means of SLAs in the eastern TP from 1995 to 2016 were distributed irregularly in the north and south. The lowest and highest values were interlaced in places that may be affected by the southern terrains. Consequently, the SLA and its variability may be attributed to various factors, such as topographic differences between the regions, apart from the climate regime.

6 Conclusions

Based on the GEE cloud-based platform, this study develops a simple but effective algorithm that adaptively separates snow from clean ice by implementing the Otsu thresholding method on the NIR band of cloudless Landsat images to delineate glacier SLAs at the end of the ablation period from 1995 to 2016. We investigate the impacts of climatic factors on the SLAs of different types of glaciers (both maritime and continental glaciers) and their variations over the period studied. The main findings are summarized as follows:

(1) The SLAs of the three regions show increasing trends during the 22-year period, with increases of 94 m 22 yr^{-1}, 55 m 22 yr^{-1}, and 49 m 22 yr^{-1} from south to north.

Maritime glaciers in the SK region are more sensitive to the local monsoon climate, with the most pronounced variation in SLA ($R^2 = 0.56$).

(2) The northern continental glaciers (BK and WQ regions) are mainly affected by temperature and the southern maritime glaciers (SK region) are influenced by precipitation. Under the impact of primary climatic factors on SLA variations, continental glaciers have higher SLA on the south slope than on the north slope, whereas maritime glaciers have higher SLA on the north slope than on the south slope. The local patterns of temperature and precipitation, which influence glaciers and their snowlines, cause not only intraregional variability but also variations between regions.

(3) The GEE platform and the approach proposed in this study have great potential to be developed further into an invaluable tool for obtaining more available satellite images to monitor SLA variability at 30 m resolution over longer periods or larger regions.

Acknowledgments

We thank the Google Earth Engine development team for input and assistance with the API code. We also thank the National Meteorological Information Centre for providing the meteorological data. This work was supported by the National Key Research and Development Program of China (No. 2018YFA0605403), the Key Deployment Program of AIRCAS under Grant Y950930Z2F, and the Science and Technology Basic Resource Investigation Program of China (No. 2017FY100502).

References

1. C. Halla et al., "Ice content and interannual water storage changes of an active rock glacier in the dry Andes of Argentina," *Cryosphere* **15**(2), 1187–1213 (2021).
2. D. Cáceres et al., "Assessing global water mass transfers from continents to oceans over the period 1948–2016," *Hydrol. Earth Syst. Sci.* **24**(10), 4831–4851 (2020).
3. M. Khadka, R. B. Kayastha, and R. Kayastha, "Future projection of cryospheric and hydrologic regimes in Koshi River basin, Central Himalaya, using coupled glacier dynamics and glacio-hydrological models," *J. Glaciol.* **66**(259), 831–845 (2020).
4. Z. Li et al., "Partitioning the contributions of glacier melt and precipitation to the 1971–2010 runoff increases in a headwater basin of the Tarim River," *J. Hydrol.* **583**, 124579 (2020).
5. A. Bhattacharya et al., "High Mountain Asian glacier response to climate revealed by multitemporal satellite observations since the 1960s," *Nat. Commun.* **12**(1), 4133 (2021).
6. F. Chen et al., "Annual 30-meter dataset for Glacial Lakes in high mountain Asia from 2008 to 2017," *Earth Syst. Sci. Data* **13**, 741–766 (2020).
7. G. Deng et al., "Spatiotemporal dynamics of snowline altitude and their responses to climate change in the Tienshan Mountains, Central Asia, During 2001–2019," *Sustainability* **13**, 3992 (2021).
8. D. E. Shean et al., "A systematic, regional assessment of high mountain Asia glacier mass balance," *Original Res.* **7**, 363 (2020).
9. L. M. Andreassen et al., "Glacier change in Norway since the 1960s: an overview of mass balance, area, length and surface elevation changes," *J. Glaciol.* **66**, 313–328 (2020).
10. G. H. Roe, M. B. Baker, and F. Herla, "Centennial glacier retreat as categorical evidence of regional climate change," *Nat. Geosci.* **10**(2), 95–99 (2016).
11. R. Braithwaite, "Can the mass balance of a glacier be estimated from its equilibrium-line altitude?" *J. Glaciol.* **30**, 364–368 (1984).
12. M. Girona-Mata et al., "High-resolution snowline delineation from landsat imagery to infer snow cover controls in a Himalayan catchment," *Water Res. Res.* **55**(8), 6754–6772 (2019).
13. A. Rabatel et al., "Can the snowline be used as an indicator of the equilibrium line and mass balance for glaciers in the outer tropics?" *J. Glaciol.* **58**(212), 1027–1036 (2012).
14. M. Bishop et al., "Remote sensing science and technology for studying glacier processes in high Asia," *Ann. Glaciol.* **31**, 164–170 (2000).

15. A. Racoviteanu, M. Williams, and R. Barry, "Optical remote sensing of glacier characteristics: a review with focus on the Himalaya," *Sensors* **8**(5), 3355–3383 (2008).
16. A. Rabatel et al., "Annual and seasonal glacier-wide surface mass balance quantified from changes in glacier surface state: a review on existing methods using optical satellite imagery," *Remote Sens.* **9**, 507 (2017).
17. B. Raup et al., "Remote sensing and GIS technology in the Global Land Ice Measurements from Space (GLIMS) Project," *Comput. Geosci.* **33**(1), 104–125 (2007).
18. A. Rabatel, J. P. Dedieu, and C. Vincent, "Using remote-sensing data to determine equilibrium-line altitude and mass-balance time series: validation on three French glaciers, 1994-2002," *J. Glaciol.* **51**(175), 539–546 (2005).
19. A. Racoviteanu, K. Rittger, and R. Armstrong, "An automated approach for estimating snowline altitudes in the Karakoram and Eastern Himalaya from remote sensing," *Front. Earth Sci.* **7**, 220 (2019).
20. P. Rastner et al., "On the automated mapping of snow cover on glaciers and calculation of snow line altitudes from multi-temporal landsat data," *Remote Sens.* **11**, 1410 (2019).
21. M. Price et al., "Mountain geography: physical and human dimensions," *Arctic Antarctic and Alpine Research* **46**(2), 525–527 (2013).
22. P. Krajčí et al., "Estimation of regional snowline elevation (RSLE) from MODIS images for seasonally snow covered mountain basins," *J. Hydrol.* **519**, 1769–1778 (2014).
23. E. M. McFadden, J. Ramage, and D. T. Rodbell, "Landsat TM and ETM plus derived snowline altitudes in the Cordillera Huayhuash and Cordillera Raura, Peru, 1986–2005," *Cryosphere* **5**(2), 419–430 (2011).
24. Z. Tang et al., "Extraction and assessment of snowline altitude over the Tibetan plateau using MODIS fractional snow cover data (2001 to 2013)," *J. Appl. Remote Sens.* **8**, 084689 (2014).
25. Z. Tang et al., "Spatiotemporal variation of snowline altitude at the end of melting season across High Mountain Asia, using MODIS snow cover product," *Adv. Space Res.* **66**(11), 2629–2645 (2020).
26. S. H. Winsvold, A. Kääb, and C. Nuth, "Regional glacier mapping using optical satellite data time series," *IEEE J. Sel. Top. Appl. Earth Obs. Remote Sens.* **9**(8), 3698–3711 (2016).
27. S. H. Park, M. J. Lee, and H. S. Jung, "Spatiotemporal analysis of snow cover variations at Mt. Kilimanjaro using multi-temporal Landsat images during 27 years," *J. Atmos. Solar-Terrest. Phys.* **143**, 37–46 (2016).
28. O. King et al., "Spatial variability in mass change of glaciers in the Everest region, central Himalaya, between 2000 and 2015," *Cryosphere* **11**, 407–426 (2017).
29. Z. Hu, A. Dietz, and C. Kuenzer, "The potential of retrieving snow line dynamics from Landsat during the end of the ablation seasons between 1982 and 2017 in European mountains," *Int. J. Appl. Earth Obs. Geoinf.* **78**, 138–148 (2019).
30. J. Dozier, "Remote sensing of alpine snow cover in visible and near-infrared wavelengths," *presented at the Annu. Rev. Earth and Planet. Sci.* (1992).
31. Z. Guo et al., "Temporal and spatial changes in Western Himalayan firn line altitudes from 1998 to 2009," *Global Planet. Change* **118**, 97–105 (2014).
32. B. G. Mark et al., "Tropical snowline changes at the last glacial maximum: a global assessment," *Quarter. Int.* **138**(3), 168–201 (2005).
33. T. Yao, *Map of Glaciers and Lakes on the Tibetan Plateau and Adjoining Regions*, Xi'an Cartographic Publishing House, Xi'an (2008).
34. Y. Ageta and T. Kadota, "Predictions of changes of glacier mass balance in the Nepal Himalaya and Tibetan Plateau: a case study of air temperature increase for three glaciers," *Ann. Glaciol.* **16**, 89–94 (1992).
35. K. Fujita et al., "Superimposed ice in glacier mass balance on the Tibetan Plateau," *J. Glaciol.* **42**(142), 454–460 (1996).
36. T. Bolch et al., "A glacier inventory for the western Nyainqentanglha Range and the Nam Co Basin, Tibet, and glacier changes 1976–2009," *Cryosphere* **4**(3), 419–433 (2010).
37. N. Otsu, "A threshold selection method from gray-level histograms," *IEEE Trans. Syst. Man Cybern.* **9**, 62–66 (1979).

38. C. R. A. Clarke, "Three journeys to high altitude: medicine, Tibetan thangkas, and Sepu Kangri," *J. R. Coll. Phys. Lond.* **33**, 78–84 (1999).
39. Q. Liu et al., "Recent glacier and glacial lake changes and their interactions in the Bugyai Kangri, southeast Tibet," *Ann. Glaciol.* **57**(71), 61–69 (2016).
40. N. Gorelick et al., "Google Earth Engine: planetary-scale geospatial analysis for everyone," *Remote Sens. Environ.* **202**, 18–27 (2017).
41. China Meteorological Data Service Centre, http://data.cma.cn/ (accessed 13 July 2017).
42. N. Chrysoulakis et al., "Validation of ASTER GDEM for the Area of Greece," *Photogramm. Eng. Remote Sens.* **77**(2), 157–165 (2011).
43. A. Chen et al., "The variations of firn line altitude on the Binglinchuan Glacier, Ulugh Muztagh during 2000-2013," *J. Glaciol. Geocryol.* **36**(5), 1069–1078 (2014).
44. M. P. Bishop et al., "Global Land Ice Measurements from Space (GLIMS): remote sensing and GIS investigations of the Earth's cryosphere," *Geocarto Int.* **19**(2), 57–84 (2004).
45. RGI Consortium, "Randolph Glacier Inventory - A Dataset of Global Glacier Outlines: Version 6.0: Technical Report," Global Land Ice Measurements from Space, Colorado, USA. Digital Media (2017).
46. D. K. Hall et al., "Characterization of snow and ice reflectance zones on glaciers using landsat thematic mapper data," *Ann. Glaciol.* **9**, 104–108 (1987).
47. R. Gonzalez and R. Woods, *Digital Image Processing*, Vol. 12, Pearson Education (2008).
48. H. De Angelis, "Hypsometry and sensitivity of the mass balance to changes in equilibrium-line altitude: the case of the southern Patagonia Icefield," *J. Glaciol.* **60**(219), 14–28 (2014).
49. L. M. Andreassen et al., "Landsat-derived glacier inventory for Jotunheimen, Norway, and deduced glacier changes since the 1930s," *Cryosphere Discuss.* **2**, 299–339 (2008).
50. A. Racoviteanu et al., "Decadal changes in glacier parameters in the Cordillera Blanca, Peru, derived from remote sensing," *J. Glaciol.* **54**, 499–510 (2008).
51. H. Frey, F. Paul, and T. Strozzi, "Compilation of a glacier inventory for the western Himalayas from satellite data: methods, challenges, and results," *Remote Sens. Environ.* **124**(124), 832–843 (2012).
52. B. Tian et al., "Mapping Thermokarst Lakes on the Qinghai–Tibet Plateau using nonlocal active contours in Chinese GaoFen-2 multispectral imagery," *IEEE J. Sel. Top. Appl. Earth Obs. Remote Sens.* **10**(5), 1687–1700 (2017).
53. J. Liu, Z. Cheng, and Q. Li, "Meteorological conditions for frequent debris flows from Guxiang glacier, Mount Nyenchen Tanglha, China," *Mount. Res. Dev.* **33**, 95–102 (2013).
54. T. Yao et al., "Chained impacts on modern environment of interaction between Westerlies and Indian Monsoon on Tibetan Plateau," *Bull. Chin. Acad. Sci.* **9**, 976–984 (2017).

Chang Liu received her BS degree in remote sensing science and technology from Shandong University of Science and Technology, Shandong, China, in 2017. She is currently a graduate student working toward her PhD in cartography and geography information system at the Key Laboratory of Digital Earth Science, Aerospace Information Research Institute, Chinese Academy of Sciences. Her current research interests include the assessment and application of snow products and microwave remote sensing of glacier and snow.

Zhen Li received his PhD in natural geography from Lanzhou Institute of Glaciology and Geocryology, Chinese Academy of Sciences, Lanzhou, China, in 1998. He is currently a professor in the Key Laboratory of Digital Earth Science, Aerospace Information Research Institute, Chinese Academy of Sciences. He has authored more than 100 papers and has authored and coauthored four books in collaboration with others. His current research interests include microwave remote sensing and cryosphere environment.

Ping Zhang received her PhD in communication and information system from the Institute of Electronics, Chinese Academy of Sciences, Beijing, China, in 2009. Currently, she is currently an associate professor in the Key Laboratory of Digital Earth Science, Aerospace Information Research Institute, Chinese Academy of Sciences. She has authored and coauthored more than 20 articles and three book chapters. Her current research interests are remote sensing data processing, signal processing, and calibration of SAR.

Bangsen Tian received his BS degree from Wuhan University, Wuhan, China, in 2005, and his PhD in cartography and geographic information system from the Aerospace Information Research Institute, Chinese Academy of Sciences, Beijing, China, in 2010. He is currently an associate professor in the Aerospace Information Research Institute, Chinese Academy of Sciences. His research interests include synthetic aperture radar image processing and modeling scattering of electromagnetic waves for microwave remote sensing application.

Jianmin Zhou received his PhD in cartography and geographic information system from the Aerospace Information Research Institute, Chinese Academy of Sciences, Beijing, China, in 2009. He is currently an associate professor in the Key Laboratory of Digital Earth Science, Aerospace Information Research Institute, Chinese Academy of Sciences. His research interests include InSAR, glacier velocity, and mass balance change.

Quan Chen received his BS degree from Wuhan University, Wuhan, China, in 2003, and his PhD in geographic information systems from the Aerospace Information Research Institute, Chinese Academy of Sciences, Beijing, China, in 2008. He is an associate professor in the Key Laboratory of Digital Earth Science, Aerospace Information Research Institute, Chinese Academy of Sciences. His research interests include airborne remote sensing data processing and active and passive microwave remote sensing applied to hydrology.